Journal Pre-proofs

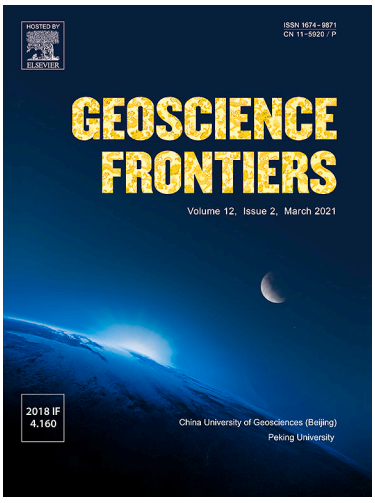

Research Paper

First observation of coexistence of crystalline and amorphous mineral phases in the Bhawad LL6 chondrite: Evidence from Micro-Raman spectroscopic studies

Bhaskar J. Saikia, G. Parthasarathy, Binoy K. Saikia, Puja Bordoloi, Rashmi R. Borah

PII: S1674-9871(25)00241-5
DOI: https://doi.org/10.1016/j.gsf.2025.102236
Reference: GSF 102236

To appear in: *Geoscience Frontiers*

Received Date: 5 July 2025
Revised Date: 23 November 2025
Accepted Date: 7 December 2025

Please cite this article as: B.J. Saikia, G. Parthasarathy, B.K. Saikia, P. Bordoloi, R.R. Borah, First observation of coexistence of crystalline and amorphous mineral phases in the Bhawad LL6 chondrite: Evidence from Micro-Raman spectroscopic studies, *Geoscience Frontiers* (2025), doi: https://doi.org/10.1016/j.gsf.2025.102236

Research Paper

First observation of coexistence of crystalline and amorphous mineral phases in the Bhawad LL6 chondrite: Evidence from Micro-Raman spectroscopic studies

Bhaskar J. Saikia[a,*], G. Parthasarathy[b,c], Binoy K. Saikia[d], Puja Bordoloi[d], Rashmi R. Borah[e]

[a] Department of Physics, Anandaram Dhekial Phookan College, Nagaon 782002, India

[b] School of Natural and Engineering Sciences, National Institute of Advanced Studies, Indian Institute of Science Campus, Bengaluru 560012, India.

[c] Raja Ramanna Chair Professor, Atomic Minerals Directorate for Exploration & Research (AMD), Naagarabhaavi, Bengaluru 560072, India.

[d] Coal and Energy Division, CSIR-North East Institute of Science and Technology, Jorhat 785006, India

[e] Department of Physics, Nagaon University, Nagaon 782001, India

*Corresponding author email address: vaskaradp@gmail.com

Abstract

We report here for the first time the detailed spectroscopic investigations on Bhawad meteorite using micro-Raman spectroscopic and high-resolution transmission electron microscopy (HR-TEM) investigation of the Bhawad LL6 ordinary chondrite, focusing on its mineralogical composition and carbonaceous phases. Raman spectroscopy reveals crystalline silicates including olivine, pyroxene, and plagioclase, along with accessory chromite containing ≤ 20% of Al. Carbonaceous material exhibits broad I_D (~1336 cm^{-1}) and I_G (~1587 cm^{-1}) bands with an I_D/I_G ratio of ~1.04, indicative of disordered graphite and nanocrystalline carbon, reflecting shock-induced metamorphism. High-pressure TiO_2 polymorphs are identified by characteristic Raman modes at 146, 394, 446, and 610 cm^{-1}. HR-TEM imaging confirms the presence of nanocrystalline TiO_2 particles embedded within amorphous carbonaceous matrices, demonstrating the coexistence of crystalline and amorphous phases. The Raman spectra of the Bhawad meteorite reveal the presence of high-temperature plagioclase phases, characterized by these distinct vibrational features. This observation indicates possible quenching of the melts having feldspar components, representing the complex thermal and shock metamorphic history of the meteorite. This coexistence of

crystalline and amorphous phases highlights the complex thermal and shock history of the Bhawad meteorite, revealing insights into phase transitions and structural order-disorder phase transition induced by impact processes.

Keywords: Bhawad chondrite, Silicates, Carbonaceous material, Raman spectroscopy

1. Introduction

Meteorites are key extraterrestrial materials, providing crucial information on the formation and early evolution of the solar system through their chemical, physical, and textural properties (McSween, 1999). Thousands of meteorites fall to Earth annually, with over 25,000 fragments recovered from hot and cold deserts (Meteoritical Society Database); However, many samples are altered by terrestrial weathering and contamination prior to recovery (Lee and Bland, 2004; Mahajan, 2017). Pre-solar particles, such as micro-diamond, nano-crystalline graphite, SiC, and Al_2O_3, offer valuable insights into the processes occurring in stellar interiors and interstellar environments. In addition to providing insights into the formation and evolution of planets and smaller bodies, meteorites offer valuable information on processes within stars, interstellar regions, and the origins of life (Lewis et al., 1987; Ott, 1993; Huss and Lewis, 1995; McSween, 1999; Anfinogenova and Anfinogenov, 2019; Saikia, 2020). However, only few research groups are working on the spectroscopic characterization of chondritic meteorites. Basically, chondrites are ultramafic, chemically primitive rocks composed mainly of iron, magnesium, silicon, and oxygen, and are characterized by chondrules - spherical inclusions formed in the early solar nebula. They are regarded as the oldest rocks in the solar system (Wasson, 1974; Saikia, 2020).

Chondrites are undifferentiated stony meteorites classified into ordinary, carbonaceous, and enstatite types, further subdivided into twelve subgroups based on mineralogical and geochemical characteristics (Wasson, 1974; Wasson and Kallemeyn, 1988; Kallemeyn et al., 1996; Hutchison, 2004). Classification of chondrite groups is primarily based on variations in ferrous, metallic, and total iron content, along with differences in the Fe/Ni ratio within the metal phase (Dodd et al., 1967; Kallemeyn et al.,1989; Hutchison, 2004). Investigations of chondrites provide essential insights into the thermal histories and impact-driven processes that occurred during planetesimal collisions in the early solar system (Stöffler et al., 1991; Rubin, 1992,1995; Kerr, 2013). Ordinary chondrites constitute the most abundant class of meteorites, comprising the majority of documented falls and recovered samples on Earth. Generally, ordinary chondrites are subdivided into H, L, and LL groups based on their total iron and metallic iron content: H chondrites have high total Fe (FeO as Fe and metallic Fe), L chondrites have lower total Fe, and LL chondrites contain the lowest metallic Fe and relatively low total Fe (Agarwal et al., 2014). Our earlier studies on ordinary chondrites indicate that the Kamargaon (L6) chondrite was subjected to intense shock conditions, as demonstrated by the coexistence of ringwoodite and wadsleyite, high-pressure phases that form near the wadsleyite–ringwoodite transition boundary at ~18 GPa and 1800 K (Saikia et al., 2022a). The thermodynamic and electrical properties of ordinary chondrites indicate that they remain stable up to 1000 K and lack hydrous or organic compounds (Parthasarathy and Sharma, 2004). Phase transformations from olivine to ringwoodite and plagioclase to maskelynite have also been identified in the Natun Balijan (L4) chondrite using micro-Raman and infrared spectroscopy (Saikia et al., 2020, 2022b). On the other hand, infrared and Raman spectroscopic analyses of the ordinary chondrites viz. Dergaon (H5), Mahadevpur (H4/5), Kamargaon (L6), and Natun

Balijan (L4) have revealed the presence of nanodiamonds and organic compounds (Saikia et al., 2009a, 2017a, 2017b, 2018a, 2020, 2022a, 2022b, 2024). This study reports the mineralogical characteristics of the Bhawad (LL6) chondrites.

The Bhawad meteorite fell at Bhawad village, Jodhpur district, Rajasthan (26°30′30″N, 73°06′55″E), India on June 6, 2002 (Connolly et al., 2007). The petrographic and Mossbauer studies of Bhawad meteorite carried out by Paliwal et al. (2002) indicate that the meteorite belongs to petrographic grade 6 (Paliwal et al., 2002). The chemical and cosmogenic effects analyses of Bhandari et al. (2005) confirm that the Bhawad meteorite belongs to the LL6 group of chondrites (Bhandari et al., 2005). The Bhawad meteorite belongs to the LL6 group of ordinary chondrites, characterized by low total iron content and low metallic iron, with a high degree of thermal metamorphism corresponding to petrologic type 6. The composition of orthopyroxene has a ferrosilite (Fs) content of ~23 to 25 mol%. These compositions are in agreement with the chondrite class of LL. Bhawad represents one of the six classified LL6 ordinary chondrites reported from India. The other documented LL6 chondrites from the region include Segowlie (1853), Dhurmsala (1860), Manbhoom (1863), Sabrum (1999), and Sulagiri (2008). We followed the methodology of Kallemeyn et al. (1989) in classifying the petrographic type of the Bhawad meteorite (Kallemeyn et al., 1989). The restricted number of LL6 falls and finds from India highlights the limited representation of this meteorite group within the regional meteoritic inventory. Raman spectroscopy is a highly sensitive technique for characterizing the structures of complex transition-metal oxides, applicable to both bulk phases and surface environments (Hardcastle and Wachs, 1991). To the best of our knowledge, no prior Raman spectroscopic or infrared spectroscopic investigations have been conducted on the Bhawad meteorite. In the present study, we report, for the first time, the mineralogical composition and the occurrence of both crystalline and amorphous phases within the Bhawad meteorite. Particular emphasis is placed on the identification of silicate and carbonaceous phases, characterized through the integrated application of Raman spectroscopy and high-resolution Transmission Electron Microscopy (HR-TEM) analyses.

2. Experimental

The structural characterization of Bhawad meteorite was carried out using a High-Resolution Transmission Electron Microscope (HR-TEM), specifically the JEM 2100 Plus model (JEOL Co., Ltd., Japan), operated at an accelerating voltage of 120 kV. For HRTEM analysis, the sample was first prepared by dispersing a few milligrams in iso-propyl alcohol. This dispersion was subjected to ultrasonication for duration of 7–8 h to ensure uniform suspension of particles. Following sonication, approximately 2–3 µL of the resulting sample dispersion was extracted using a 10 µL micropipette and drop-casted (single drop) onto a copper TEM grid. The grid had been carefully placed on a clean petri dish cover, cushioned with tissue paper to avoid contamination. The sample was allowed to air-dry for a few minutes and subsequently left undisturbed overnight in a vacuum desiccator to ensure complete evaporation of the solvent. The dried grid was then analysed under HR-TEM the following day.

Raman spectroscopic analyses were performed on bulk powdered samples of the Bhawad meteorite using a Jobin-Yvon Horiba LabRam-HR Micro-Raman spectrometer (Horiba Scientific, USA) equipped with an Olympus optical microscope fitted with 10×, 50×, and 100× objectives with spot size ~ 0.5 to 2 µm. Nd:YAG laser operating at a wavelength of 532 nm with a power of ~5 mW was used as the excitation source. Powdered sample was

selected for the present investigation instead of polished thin section, as the latter will have textural and crystallite orientation effects in spectroscopic and powder XRD studies. A motorized x–y stage is included in this arrangement and used 1800 grooves mm^{-1} grating in the range from 100 to 3000 cm^{-1}. A silicon wafer (520.7 ± 0.5 cm^{-1}) was applied for calibration. The excellent accuracy (±0.5 cm^{-1}) and precision (±0.1 cm^{-1}) of peak positions for this instrument over the whole Raman spectral range make it relatively straightforward to use this technique to identify minerals based on their spectral signatures. An edge filter was applied to accurately isolate Stokes Raman scattering lines. Spectra were acquired at room temperature (28 °C) with counting times ranging from 10 to 60 s, depending on signal intensity and sample fluorescence. Data processing involved baseline correction and Gaussian curve fitting to determine the precise peak positions. Mineral phase identifications were established by comparing the observed Raman band positions to reference spectra for end-member mineral compositions at ambient pressure and temperature, as available in the RRUFF database (http://rruff.info/).

3. Results and discussion

High-Resolution Transmission Electron Microscopy (HR-TEM) analyses conducted at magnifications corresponding to 200 nm, 100 nm, and 50 nm (Fig. 1a–c) reveal that the Bhawad meteorite sample exhibits a well-defined sheet-like microstructural morphology. This morphological characteristic is indicative of a stratified or planar arrangement of its constituent mineral phases, potentially reflecting primary accretionary processes or subsequent metamorphic alteration events. In contrast, at higher imaging resolutions of 20 nm, 10 nm, and 5 nm, as depicted in Fig. 1a–f, reveal the presence of well-defined crystalline lattice fringes exhibiting random crystallographic orientations, indicative of a polycrystalline microstructure with no apparent preferred orientation. The presence of randomly oriented crystalline planes observed at higher resolutions signifies a polycrystalline microstructure in the Bhawad meteorite, possibly indicating its complex thermal and deformation history. Energy Dispersive X-ray Spectroscopy (EDS) analyses were conducted to determine the elemental composition of the meteorite sample. The spectra associated with identified accessory phases are not shown here. The presence of comparatively high carbon and oxygen contents in the EDS spectra is indicative of higher abundance of organic matter within the Bhawad meteorite sample. The presence of trace concentrations of elements including F, Mg, Al, Si, K, Ca, Ti, and Fe may contribute to the development of the dark agglomerated regions underlying the crystalline fringes in Fig. 1d and e, possibly reflecting localized compositional heterogeneity or nanoscale phase accumulation.

Crystalline phases are characterized by distinct *d*-spacing values, which serve as structural markers for phase identification. In this study, interplanar spacings were systematically measured over a 5 nm scale in multiple regions exhibiting well-defined crystalline fringes. The fringe spacings were quantified using ImageJ software, and the resulting *d*-spacing values were compared against standard reference data to facilitate phase identification and validate the presence of specific crystalline components within the meteorite sample. The interplanar *d*-spacings measured at multiple regions, with a spatial resolution of up to 5 nm, were found to range between 0.65 and 0.69 nm (6.5–6.9 Å), approximating an average value of ~7 Å, as depicted in Fig. 2a. These *d*-spacing values were derived by measuring the total distance between two parallel crystalline lattice planes, as shown in Fig. 2b, and subsequently dividing this value by the number of periodic lattice fringes, corresponding to intensity maxima, identified in the associated Gray Value versus Distance

(nm) intensity profile presented in Fig. 2c. This approach facilitates precise quantification of interplanar spacings within nanoscale crystalline domains. The *d*-spacing was also derived from the Selected Area Electron Diffraction (SAED) pattern, wherein the discrete, dot-like diffraction spots observed in Fig. 3a corroborate the polycrystalline aggregates of several crystalline-phases in the studied Bhawad meteorite. A *d*-spacing value of 3.26 Å was calculated from the SAED data by measuring the average radial distance corresponding to the diffraction rings or spots, as illustrated in the Gray Value versus Spatial Frequency (1/nm) intensity profile in Fig. 3b, and dividing this measurement by the number of diffraction peaks resolved within the pattern.

This significant variation in the measured *d*-spacing values is indicative of structural heterogeneity within the meteorite sample, likely arising from the coexistence of multiple crystalline phases or crystallographic domains. The *d*-spacing of approximately 7 Å is consistent with basal spacings characteristic of Fe-rich phyllosilicates, while the 3.26 Å spacing detected in the SAED pattern may result from diffraction along a different set of lattice planes within the same phase, a crystallographically distinct orientation, or the presence of a separate, compositionally or structurally distinct mineral phase such as a nanocrystalline oxide with distinct lattice parameters within the Bhawad meteorite. Based on previously reported literature, *d*-spacing of ~0.325 nm or 3.25 Å is characteristic of the rutile phase of TiO_2, typically corresponding to the (110) crystallographic plane (Lv et al. 2018).

The mineral compositions of the Bhawad meteorite have been published elsewhere (Bhandari et al., 2005). Olivine exhibits SiO_2 contents of 37.4–37.7 wt.%, with minor Al_2O_3 (0.02–0.04 wt.%), TiO_2 (0.02–0.03 wt.%), MnO (0.38–0.45 wt.%), CaO (0.02–0.06 wt.%), and Cr_2O_3 (0.04–0.06 wt.%). Corresponding FeO and MgO concentrations range from 24.1–25.7 wt.% and 37.0–38.0 wt.%, respectively. Orthopyroxene compositions show SiO_2 values of 55.0–55.4 wt.%, with subordinate Al_2O_3 (0.16–0.19 wt.%), TiO_2 (0.07–0.17 wt.%), MnO (0.42–0.45 wt.%), Na_2O (0.01–0.02 wt.%), and Cr_2O_3 (0.13–0.15 wt.%). FeO ranges from 14.9–15.3 wt.%, while MgO varies between 28.3 wt.% and 29.0 wt.%. CaO contents fall between 0.42 wt.% and 0.54 wt.%. The analyzed sample contains olivine with Fa(27.0–28.4) mol% and pyroxene with Fs(22.6–23.5) mol%, confirming its classification as an LL-type ordinary chondrite. Raman spectra of ferrosilite display vibrational features typical of pyroxene, including dominant Si–O stretching modes above 800 cm^{-1}, Si–O bending modes between 500 and 700 cm^{-1}, and low-frequency bands corresponding to SiO_4 rotational and metal–oxygen translational modes.

Figure 4 illustrates the Raman spectra of olivine, identified as a major mineral phase within the Bhawad meteorite sample. The olivine structure, characterized by orthorhombic *Pnma* symmetry, is predicted based on factor group analysis to exhibit 36 Raman-active vibrational modes: $11A_g + 11B_{1g} + 7B_{2g} + 7B_{3g}$ (Chopelas, 1991; Mouri and Enami, 2008; Breitenfeld et al., 2018). In Raman spectral region 100–1200 cm^{-1}, five characteristic peaks for olivine [$(Mg, Fe)_2SiO_4$] are generally registered at 826–819 cm^{-1} (peak 1), 858–849 cm^{-1} (peak 2), 883–881 cm^{-1} (peak 3), 920–914 cm^{-1} (peak 4), and 967–951 cm^{-1} (peak 5). These characteristic peaks for olivine (forsterite), peak 1, peak 2, and peak 5 are assigned to the A_g symmetry, peak 3 to B_{2g} symmetry, and peak 4 to B_{3g} symmetry. Forsterite (Mg_2SiO_4) is indicated by the Raman peaks that have been detected in the Bhawad spectra at 819, 851, 916, and 948 cm^{-1} (Fig. 4). The coupling between the symmetric (ν1) and anti-symmetric (ν3) stretching modes of $Si–O_{nb}$ bonds in SiO_4 tetrahedra is responsible for the doublet that is detected at 819 cm^{-1} and 851 cm^{-1} in the Bhawad spectrum (Saikia et al., 2009a, 2009b, 2009c, 2017a, 2017b, 2017d, 2018a, 2018b, 2022a, 2022b, 2022c, 2024). The relative positions and

intensity ratio of this doublet are sensitive to both the fayalite (Fa) and forsterite (Fo) content in olivine, as well as the crystallographic orientation of the analyzed grains (Mouri and Enami, 2008; Breitenfeld et al., 2018). The observed Raman doublet peak separation of Δ = 28 to 32 cm^{-1} suggests that the olivine composition is approximately $Fo_{76\text{-}70}Fa_{24\text{-}30}$ (Kuebler et al., 2006; Mouri and Enami, 2008; Breitenfeld et al., 2018), which agrees well with the previous compositional data.

The Raman spectrum of Bhawad meteorite shows strong peaks at 1006, 680, 661, and 338 cm^{-1} in the Raman spectral characteristic ranges (~1000 cm^{-1}, ~ 670 cm^{-1}, and 400–200 cm^{-1}) of pyroxene (Fig. 5). These characteristic Raman lines belong to orthopyroxene mineral component. As orthopyroxene and clinopyroxene exhibit similar Raman spectral features (Mouri and Enami, 2008; Breitenfeld et al., 2018), the presence of a small clinopyroxene component cannot be ignored. In general, the frequencies of Raman peaks in these locations progressively change with Mg/Fe and Wo concentration in pyroxenes. The Raman bands at 1006, 680, and 661 cm^{-1} correspond to the stretching $\nu(Si\text{-}O_{nb})$ and $\nu(Si\text{-}O_b\text{-}Si)$. The 1006 cm^{-1} band attributed to the $Si–O_{nb}$ stretching (where O_{nb} is non-bridging oxygen), while the bands at 680 cm^{-1} and 661 cm^{-1} correspond to $Si–O_b–Si$ stretches (where O_b is bridging oxygen connecting adjacent SiO_4 tetrahedra), characteristic of the two oxygen-sharing tetrahedra in the inosilicate chain structure (Yu and Wentzcovitch, 2006; Saikia et al., 2017a, 2017b, 2017c, 2018a, 2018b, 2022a, 2022b, 2022c, 2024). The peaks at 397, 480, 515, 581, 661, and 680 cm^{-1} originate from the internal bending modes ($\nu2$ and $\nu4$) of the SiO_4 tetrahedron, as well as from Si and Mg atomic displacements.

Traces of maskelynite are inferred from characteristic Raman peaks at around 515 and 581 cm^{-1}, consistent with previous spectral identifications in shocked plagioclase (Fritz et al., 2005; Jaret et al., 2014, 2015, 2018). Raman peaks at 235, 281, and 338 cm^{-1} within the low-wavenumber region (below 400 cm^{-1}) are primarily attributed to external lattice modes, encompassing the rotational and translational dynamics of SiO_4 tetrahedra, along with translational motions of divalent octahedral cations (Mg^{2+}, Fe^{2+}) within the silicate crystal lattice (Yu and Wentzcovitch, 2006). The Raman peaks at 131 and 188 cm^{-1} are indicative of cage-shear vibrational modes, involving collective shearing motions of interconnected polyhedral units within the silicate framework. Additionally, these peaks provide valuable information on temperature dependence, although their intensities are suppressed due to the limited polarizability of the octahedral structural units (Hofmeister et al., 1989; Chopelas, 1990; Yu and Wentzcovitch, 2006). Within the pyroxene spectral region, weak and broad Raman features consistent with disordered graphite were also detected, indicating the presence of carbonaceous material intermixed with silicate phases.

Characteristic Raman spectral features attributable to plagioclase were also identified in the Bhawad meteorite (Fig. 6). The Raman spectra is characterized by a prominent doublet at 480 and 511 cm^{-1}, attributed to the Si–O–Si symmetric stretching vibrations within the aluminosilicate framework, accompanied by a weaker peak at 285 cm^{-1}, associated with lattice vibrational modes of the plagioclase structure. Plagioclase represents a continuous solid solution series between albite (Ab; $NaAlSi_3O_8$) and anorthite (An; $CaAl_2Si_2O_8$), with the extent of solid solution governed by the coupled substitution of Na^+ and Ca^{2+} ions within the tetrahedral framework. The observed Raman features were systematically compared with previously published spectral data for plagioclase phases in various ordinary chondrites (Wang et al., 2004; Pittarello et al., 2015; Bersani et al., 2018) indicates that the plagioclase composition in the Bhawad meteorite closely resembles that of the Chelyabinsk LL5 chondrite (Kaeter et al., 2018). Based on the relative positions and intensities of the diagnostic Raman

bands, the plagioclase phase in the Bhawad meteorite is estimated to have a composition of approximately $An_{27}Ab_{73}$.

Figure 7 displays the Raman spectrum corresponding to the chromite phase identified within the Bhawad meteorite. This structural configuration gives rise to characteristic Raman-active modes, particularly including the prominent A_{1g} and F_{2g} vibrations associated with the Cr–O stretching within the octahedral framework. In chromite-group minerals, substitution of Cr^{3+} by Al^{3+}within the octahedral sites leads to a progressive shift of the characteristic A_{1g} mode from ~680 cm^{-1} in pure chromite toward higher wavenumbers, typically approaching ~690 cm^{-1}, depending on Al content (Wang et al., 2004). In the present analysis, a broad Raman band centered at 685 cm^{-1} is observed, corresponding to the A_{1g} symmetric stretching vibration of Cr–O bonds within (Cr^{3+}, Fe^{3+}, Al^{3+})O_6 octahedral units in the spinel lattice. Additionally, a distinct Raman peak at 573 cm^{-1} is attributed to the F_{2g} vibrational mode, representing antisymmetric stretching of the same octahedral units. Moreover, the Raman peak at 500 cm^{-1} is assigned to the F_{2g} *(2)* vibrational mode, corresponding to the bending and coupled lattice vibrations of oxygen atoms in the octahedral site. The relative positions and intensities of these diagnostic Raman bands suggest that the aluminium content in the chromite phase of the Bhawad meteorite is moderate, not exceeding ~ 20% (Pittarello et al., 2015). These results are consistent with reported chromite compositions in other equilibrated ordinary chondrites and contribute to constraining the petrogenetic history and metamorphic conditions experienced by the Bhawad meteorite.

The Raman spectra of carbonaceous material associated with accessory phases in the Bhawad meteorite are presented in Fig. 8. The spectra display broad and prominent bands within the 1100–1800 cm^{-1} range, characteristic of structurally disordered and nanocrystalline carbonaceous matter. In amorphous carbon, all three bonding configurations *sp*, sp^2, and sp^3 hybridizations can coexist, whereas crystalline graphite predominantly exhibits sp^2 bonding. In crystalline graphite, the largest peak is detected at 1581 cm^{-1} (G band), which corresponds to framework vibrations in the graphene layers with sp^2 hybridized valent bonds. In the Bhawad sample, the G band is slightly upshifted to 1587 cm^{-1}, indicating the presence of well-ordered crystalline graphite. A prominent peak in the Raman spectrum of disordered and microcrystalline graphite is located at around 1350 cm^{-1} (D band). This peak is also prominent in the spectra of amorphous and nanocrystalline carbon. In the Raman spectrum of Bhawad, this D band is observed at 1336 cm^{-1}. A clear evidence of complex D band reveals in Fig. 9. It comprises of multiple bands associated with the presence of distinct crystallite borders at 1336 cm^{-1} that are referred to as the band D1 of the disordered carbon network. Another band observed at 1620 cm^{-1} near the G band is referred as band D2. The band found at 1540 cm^{-1} corresponding to amorphous carbon is referred as band D3. The forth band observed at ~ 1200 cm^{-1} is referred as band D4 that related to the sp^3 bonds or C–C and C=C stretch vibrations of polyene-like structures (Marshall et al., 2010). The Bhawad meteorite sample exhibited the characteristic D3 and D4 bands of nanocrystalline and glassy carbon. In addition to these first-order Raman bands, broad, low-intensity features are also observed in the higher-frequency region at ~ 1800 cm^{-1} and ~1920 cm^{-1}. These are attributed to second-order Raman processes involving overtones and combination modes of the fundamental vibrational bands within the carbonaceous network. The relatively weak intensities of these Raman bands, accompanied by significant background fluorescence, suggest interference effects likely related to the presence of amorphous, or nanocrystalline carbon phases, structural disorder, or fine-grained material within the sample. Moreover, the variation in Raman spectral features (Figs. 8 and 9) reflect the heterogeneous distribution of carbonaceous matter within the Bhawad meteorite, encompassing both crystalline graphite and disordered, nanocrystalline to amorphous carbon,

317 indicative of variable graphitization levels and complex thermal histories. Dodd et al. (1985)
318 have observed the shock melt glasses in the Bloomington LL-group chondrite, that were
319 examined using electron-beam microscopy. The observation of glassy materials in LL6
320 meteorite is established through electron microscopy (Dodd et al., 1985). However, the present
321 study represents application of micro-Raman spectroscopy in observation of glassy/amorphous
322 phase in Bhawad (LL6 meteorite).

323 The positions, intensities, and relative bandwidths of the characteristic D and G bands
324 in Raman spectra serve as sensitive indicators for assessing the structural ordering and degree
325 of crystallinity in carbonaceous materials (El Goresy et al., 2001; Saikia et al., 2017a). To
326 minimize background fluorescence, Raman spectra were processed using a least-squares
327 moving average baseline correction, enabling accurate determination of full width at half
328 maximum (FWHM) values. The reliability of this approach is supported by consistent
329 applications in the characterization of carbonaceous phases across a range of shock
330 metamorphic environments (El Goresy et al., 2001; Mostefaoui et al., 2002; Gucsik et al.,
331 2008). The calculated FWHM for the D peak (~75 cm^{-1}) falls within the 10–120 cm^{-1} range
332 typical of shock-induced diamonds, suggesting the occurrence of shock metamorphism in the
333 meteorite sample (Miyamoto et al., 1998).The relative intensities of the ~1336 cm^{-1} (I_D) and
334 ~1587 cm^{-1} (I_G) peaks, combined with their FWHM values, provide critical insight into the
335 degree of graphitization and the effects of thermal and shock metamorphism experienced by
336 the carbonaceous matter. Wopenka et al. (2013) defined the intensity ratio of the Raman
337 diamond (I_D) and graphite (I_G) peaks in graphitic carbon, with $I_D/I_G < 0.5$ indicating well-
338 ordered graphite, $0.51 < I_D/I_G < 1.1$ corresponding to disordered graphite, and $I_D/I_G > 1.1$
339 signifying glassy carbon (Wopenka et al. 2013). The calculated I_D/I_G ratio of ~1.04 for the
340 Bhawad meteorite suggests the predominance of disordered graphite within the sample,
341 indicative of partial graphitization potentially driven by impact-induced shock metamorphism
342 and post-shock thermal events. This finding aligns with previous observations of carbonaceous
343 phases in other chondritic meteorites subjected to varying degrees of shock and thermal
344 alteration.

345 High-pressure polymorphs of titanium dioxide (TiO_2) were detected within the
346 carbonaceous phases and associated accessory minerals of the Bhawad meteorite (Fig. 9).
347 Raman active phases of titanium dioxide are usually observed in the 100–900 cm^{-1} region
348 (Porto et al., 1967; Deo et al., 1992; Lukacevic et al., 2012). In meteorites, titanium oxide
349 polymorphs such as rutile, anatase, and brookite are found. On the other hand, high-pressure
350 rutile polymorph with an α–PbO_2 type structure was found in the German meteoritic crater Rais
351 (El Goresy et al., 2001a). Structurally, rutile and anatase crystallize in a tetragonal system,
352 belonging to space groups D_{4h}^{14} and D_{4h}^{19} respectively, while brookite adopts an orthorhombic
353 structure with space group D_{2h}^{15} , thus exhibiting lower symmetry than rutile and anatase
354 (Ohsaka et al., 1978; Arsov et al., 1991; Ma et al., 2007). There are 15 optical modes for
355 anatase, and they have the normal vibrations: $1A_{1g}+1A_{2u}+2B_{1g}+1B_{2u}+3E_g+2E_u$ (Sekiya et al.,
356 2001), in which the $1A_{1g}$, $2B_{1g}$, and $3E_g$ symmetries are represent six Raman active modes
357 (Porto et al., 1967). However, the two TiO_2 units in the unit cell in rutile imply 15 vibrational
358 modes as: $1A_{1g}+1A_{2g}+1A_{2u}+1B_{1g}+1B_{2g}+2B_{1u}+1E_g+3E_u$ (Porto et al., 1967; Lukacevic et al.,
359 2012), where B_{1g}, E_g, A_{1g}, and B_{2g} are the four symmetric Raman active modes of rutile (Porto
360 et al., 1967). According to factor group analysis, there are 69 optical modes for brookite, and
361 they have the irreducible representation of normal vibrations
362 $9A_{1g}+9B_{1g}+9B_{2g}+9B_{3g}+9A_{1u}+8B_{1u}+8B_{2u}+8B_{3u}$ (Tompsett et al., 1995). The A_{1u} mode is
363 inactive in both Raman and infrared, but the remaining 36 anticipated modes, represented by
364 A_{1g}, B_{1g}, B_{2g}, and B_{3g}, are active in Raman (Tompsett et al., 1995). The detection of high-

pressure TiO_2 polymorphs within the Bhawad meteorite, particularly within carbonaceous phases, which is further supported by the *d*-spacing of 3.26 Å observed in the SAED pattern, along with the presence of titanium (0.85 wt.%) detected in the EDS spectrum obtained from HRTEM analysis, provides additional evidence of impact-related metamorphic conditions capable of stabilizing these phases. These results are consistent with previous Raman studies of shocked meteorites and terrestrial impact spherules during Neoarchean (Smith et al. 2016). Smith et al. (2016) have made a discovery, using micro-Raman spectroscopy, of shock-induced TiO_2-II, a high-pressure polymorph of TiO_2, in 34 grains from four Neoarchean spherule layers deposited between ca. 2.65 Ga and 2.54 Ga. As all the TiO_2-II-bearing grains contain rutile, they interpret them as shock-metamorphosed rutile grains. Gorecy et al. (2001) have discovered high-pressure phase of rutile with Seven-Coordinated Titanium from the Ries Crater an impact structure (El Goresy et al., 2001b). The cell parameters are as follows: a = 4.606(2) angstroms, b = 4.986(3) angstroms, c = 4.933(3) angstroms, β (angle between c and a axes) = 99.17(6)°; space group P2 1/c; density = 4.72 g/cm^3. This high-pressure phase is 11% denser than rutile. The presence of baddeleyite-type TiO_2 in the shocked rocks indicates that the peak shock pressure was between 16 and 20 gigapascals, and the post-shock temperature was much lower than 500 °C.

The Raman spectrum of the Bhawad meteorite exhibits prominent peaks at 146, 256, 330, 394, 446, 610, and 645 cm^{-1} (Fig. 9). These Raman peaks are interpreted as arising from a mixture of TiO_2 polymorphs that have undergone structural modifications under high-temperature and high-pressure conditions, reflecting shock metamorphic effects within the meteorite. The Raman modes E_g, B_{1g} and the A_{1g} are correspondingly associated with the symmetric stretching vibration, the symmetric bending vibration and the anti-symmetric bending vibration of O-Ti-O bonds (Yan et al., 2013; Zhang et al., 2013). The intensity and positions of these vibrational modes are influenced by the crystallinity, as well as the pressure and temperature conditions during oxide formation (Yan et al., 2013; Zhang et al., 2013). However, as the crystallite size decreases, rutile shows Raman shift in the vibrational modes A_{1g} and E_g, that can be attributed to the three-dimensional phonon confinement effect (Swamy et al., 2006). In the observed mixed-phase structure, the ratio of the integrated Raman peak intensities of rutile at 446 cm^{-1} (E_g mode) to anatase at 394 cm^{-1} (B_{1g} mode) provides a semi-quantitative estimate of the relative weight proportions of the rutile and anatase phases (Zhang et al., 2005). The intense Raman peak observed at 146 cm^{-1} due to E_g indicates increasing crystallinity of TiO_2 nanoparticles formed under high-pressure and high-temperature conditions. Additionally, non-stoichiometric effects in TiO_2 nanophases are responsible for a red shift in the E_g mode of rutile (Parker et al., 1990). The weak peak at 235 cm^{-1} is likely due to disorder-induced scattering or a second-order multi-phonon process (Balachandran and Eror, 1982). Moreover, rutile crystals typically exhibit dominant peaks in the ranges of 445.8–447.0 cm^{-1} and 609.8 – 612.0 cm^{-1} (Arsov et al., 1991; Ma et al., 2007; Ekoi et al., 2017), consistent with the peaks at 446 and 610 cm^{-1} observed in the Bhawad meteorite, corresponding to the E_g and A_{1g} modes of rutile respectively.

Figure 10 depicts the broad Raman bands characteristic of chemically heterogeneous glass, consistent with observations reported by Matson et al. (1986) and Fagan et al. (2000). However, plagioclase glasses typically exhibit Raman peaks in the 400–650 cm^{-1} range, with a prominent maximum near 490 cm^{-1}, whereas olivine glasses are marked by a distinct peak around 830 cm^{-1}. Additionally, Raman peaks between 500 and 700 cm^{-1} are diagnostic of Si-rich glasses (Matson et al., 1986; Fagan et al., 2000). In crystalline plagioclase feldspars, a characteristic A_g vibrational mode commonly occurs between 500 and 510 cm^{-1}. The broad band observed at ~ 490 cm^{-1} in the Bhawad meteorite is attributed to overlapping Si–O–Si (or

Si–O–Al) symmetric stretching vibrations, consistent with the presence of plagioclase glass. Moreover, the peaks in the range of 800–1200 cm^{-1} are attributed to bridge Si-O-Si, Si-O-Al, and Si-O end vibrations caused by silicate and aluminosilicate glasses and melts. The formation of glass occurs when isolated SiO_4 tetrahedra polymerize into complex anions, followed by intense supercooling and rapid quenching, leading to the production of disordered glass phases. The wave number ranges of 450–520 cm^{-1} exhibiting intense symmetric T-O, O-T-O, and T-O-T vibrations (T = Si, Al) and the range of cell vibrations 150–200 cm^{-1} are the most relevant for studying the feldspars structural state. The Raman spectra of the Bhawad meteorite (Fig. 6) reveal the presence of high-temperature plagioclase phases, characterized by these distinct vibrational features. This observation indicates partial melting and subsequent quenching of feldspar components, reflecting the thermal and shock metamorphic history of the meteorite.

4. Conclusion

This study presents a comprehensive microstructural and spectroscopic analysis of the Bhawad meteorite, focusing on its shock metamorphic history and associated phase transformations. Raman spectroscopy identified key mineralogical components, including olivine, pyroxene, plagioclase, chromite, carbonaceous material, and high-pressure polymorphs of TiO_2. Chromite exhibited prominent A_{1g} and F_{2g} vibrational modes, with peak positions indicating an Al content below 20%. The carbonaceous phases displayed broad I_D and I_G bands at 1336 and 1587 cm^{-1}, respectively. The calculated I_D/I_G ratio (~1.04) and D-band FWHM (~75 cm^{-1}) are diagnostic of disordered graphite produced under moderate shock pressures. The detection of additional D2 (1620 cm^{-1}), D3 (1540 cm^{-1}), and D4 (1200 cm^{-1}) bands highlights the presence of nanocrystalline and amorphous carbon, indicative of variable graphitization and shock-induced disorder. High-pressure polymorphs of TiO_2 were identified through Raman peaks at 146, 256, 330, 394, 446, 610, and 645 cm^{-1}. The intense E_g mode at 146 cm^{-1} and the prominent peaks at 446 and 610 cm^{-1} confirm the presence of rutile nanocrystals, while B_{1g} mode at 394 cm^{-1} corresponds to anatase. The rutile-to-anatase Raman intensity ratio provided a semi-quantitative estimate of relative phase proportions. The observed Raman shifts and broadened peaks reflect grain size effects, non-stoichiometry, and three-dimensional phonon confinement in nanostructured TiO_2 formed under transient high-pressure conditions. HR-TEM analyses corroborated the Raman results, revealing nanocrystalline TiO_2 grains embedded within amorphous carbon matrices. The HR-TEM also documented disordered graphite domains and turbostratic carbon, consistent with Raman-derived I_D/I_G ratios. The coexistence of nanocrystalline oxides and carbon phases within impact melt veins and along grain boundaries provides direct microstructural evidence of shock-induced phase transformation and carbon graphitization.

Acknowledgements

We are grateful to the anonymous reviewers for the most constructive comments, which have improved the manuscript. We thank Directors, Indian Institute of Technology, Guwahati (IITG) and North East Institute of Science and Technology (CSIR-NEIST) for providing experimental facilities for characterization of the meteorite. We also thank Dr. S. Sarmah, IIT Guwahati for his assistance in the micro-Raman spectroscopic analysis. GP is grateful to

Department of Atomic Energy (DAE), Government of India for supporting under DAE-Raja Ramanna Chair Scheme.

References

Agarwal, V., Parthasarathy, G., Sisodia, M.S., Bhandari, N., 2014. Fall, mineralogy and chemistry of Nathdwara H6 chondrite. Geosci. Front. 5, 413-417. http://dx.doi.org/10.1016/j.gsf.2013.07.004

Anfinogenova, Y., Anfinogenov, J., 2019. Challenges of identifying putative planetary-origin meteorites of non-igneous material. Geosci. Front. 10, 1879-1890. https://doi.org/10.1016/j.gsf.2018.11.009

Arsov, L.D., Kormann, C., Plieth, W., 1991. Electrochemical synthesis and in situ Raman spectroscopy of thin films of titanium dioxide. J. Raman Spectrosc. 22, 573–575. https://doi.org/10.1002/jrs.1250221006

Balachandran, U., Eror, N.G., 1982. Raman spectra of titanium dioxide. J. Solid State Chem. 42, 276–282. https://doi.org/10.1016/0022-4596(82)90006-8

Bersani, D., Aliatis, I., Tribaudino, M., Mantovani, L., Benisek, A., Carpenter, M.A., Gatta, G.D., Lottici, P.P., 2018. Plagioclase composition by Raman spectroscopy. J. Raman Spectrosc. 49, 684–698. https://doi.org/10.1002/jrs.5340

Bhandari, N., Murty, S.V.S., Shukla, P.N., Mahajan, R.R., Shukla, A.D., Suthar, K.M., Parthasarathy, G., Paliwal, B.S., 2005. Bhawad LL6 chondrite: Chemistry, petrology, noble gases, nuclear tracks, and cosmogenic radionuclides. Meteorit. Planet. Sci. 40, 1015–1021. https://doi.org/10.1111/j.1945-5100.2005.tb00170.x

Breitenfeld, L.B., Dyar, M.D., Carey, C.J., Tague, T.J., Wang, P., Mullen, T., Parente, M., 2018. Predicting olivine composition using Raman spectroscopy through band shift and multivariate analyses. Am. Mineral. 103, 1827–1836.

https://doi.org/10.2138/am-2018-6291

Chopelas, A., 1990. Thermal properties of forsterite at mantle pressures derived from vibrational spectroscopy. Phys. Chem. Minerals 17, 149–156.

Chopelas, A., 1991. Single crystal Raman spectra of forsterite, fayalite, and monticellite. Am. Mineral. 76, 1101–1109.

Connolly, H.C., Zipfel, J., Folco, L., Smith, C., Jones, R.H., Benedix, G., Righter, K., Yamaguchi, A., Aoudjehane, C.H., Grossman, J.N., 2007. The meteoritical bulletin, No. 91, 2007 March. Meteorit. Planet. Sci. 42, 413–466. https://doi.org/10.1111/j.1945-5100.2007.tb00242.x

Deo, G., Turek, A.M., Wachs, I.E., Machej, T., Haber, J., Das, N., Eckert, H., Hirt, A.M., 1992. Physical and chemical characterization of surface vanadium oxide supported

on titania: influence of the titania phase (anatase, rutile, brookite and B). Appl. Catal. A Gen. 91, 27–42. https://doi.org/10.1016/0926-860X(92)85176-C

Dodd, R.T., Van Schmus, W.R., Koffman, D.M., 1967. A survey of the unequilibrated ordinary chondrites. Geochim. Cosmochim. Acta 31, 921-934.

Dodd, R., Olsen, E.J., Clarke Jr, R.S., 1985. The Bloomington (LL6) chondrite and its shock melt glasses. Meteoritics 20, 575-581.

Ekoi, E.J., Stallard, C., Reid, I., Dowling, D.P., 2017. Tailoring oxide-layer formation on titanium substrates using microwave plasma treatments. Surf. Coat. Technol. 325, 299-307.

El Goresy, A., Gillet, P., Chen, M., Knstler, F., Graup, G., Stahle, V., 2001a. In situ discovery of shock-induced graphite-diamond phase transition in gneisses from the Ries Crater, Germany. Am. Mineral. 86, 611–621. https://doi.org/10.2138/am-2001-5-603

El Goresy, A, Chen, M., Dubrovinsky, L., Günther G., 2001b. An ultradense polymorph of rutile with seven-coordinated titanium from the Ries Crater. Science 293,1467-1470. https://doi.org/10.1126/science.1062342

Fagan, T., Scott, E., Keil, K., Cooney, T., Sharma, S.K., 2000. Formation of feldspathic and metallic melts by shock in enstatite chondrite Reckling Peak A80259. Meteorit. Planet. Sci. 35, 319-329. https://doi.org/10.1111/j.1945-5100.2000.tb01777.x

Fritz, J., Greshake, A., Stoffler, D., 2005. Micro-Raman spectroscopy of plagioclase and maskelynite in Martian meteorites: Evidence of progressive shock metamorphism. Antarct. Meteorite Res. 18, 96–116.

Gucsik, A., Ott, O., Marosits, E., Karczemsk, A., Kozanecki, M., Szurgot, M., 2008. Micro-Raman study of nanodiamonds from Allende meteorite. Proc. Int. Astron. Union, IAU Symposium 251, 335-340. http://dx.doi.org/10.1017/S1743921308021893

Hardcastle, F.D., Wachs, I.E., 1991. Determination of vanadium-oxygen bond distances and bond orders by Raman spectroscopy. J. Phys. Chem. 95, 5031–5041. https://doi.org/10.1021/j100166a025

Hofmeister, A.M., Xu, J., Mao, H.K., Bell, P.M., Hoering, T.C., 1989. Thermodynamics of Fe-Mg olivines at mantle pressures: Mid and far-infrared spectroscopy at high pressure. Am. Mineral. 74, 281–306.

Huss, G.R., Lewis, R.S., 1995. Presolar diamond, SiC, and graphite in primitive chondrites: Abundances as a function of meteorite class and petrologic type. Geochim. Cosmochim. Acta 59, 115-160.

Hutchison, R., 2004. Meteorites: A Petrologic, Chemical, and Isotopic Synthesis. Cambridge University Press, Cambridge, UK, 506pp.

Jaret, S.J., Kah, L.C., Harris, R.S., 2014. Progressive deformation of feldspar recording low-barometry impact processes, Tenoumer impact structure, Mauritania. Meteorit. Planet. Sci. 49, 1007–1022. https://doi.org/10.1111/maps.12310

Jaret, S.J., Woerner, W.R., Phillips, B.L., Ehm, L., Nekvasil, H., Wright, S.P., Glotch, T.D., 2015. Makselynite formation via solid-state transformation: Evidence of infrared and X-ray anisotropy. J. Geophys. Res. Planet. 120, 570–587. https://doi.org/10.1002/2014JE004764

Jaret, S.J., Johnson, J.R., Sims, M., DiFrancesco, N., Glotch, T.D., 2018. Microspectroscopic and petrographic comparison of experimentally shocked albite, andesine, and bytownite. J. Geophys. Res. Planet. 123, 1701–1722. https://doi.org/10.1029/2018JE005523

Kaeter, D., Ziemann, M.A., Bottger, U., Weber, I., Hecht, L., Voropaev, S.A., Korochantsev, A.V., Kocherov, V., 2018. The Chelyabinsk meteorite: New insights from a comprehensive electron microscopy and Raman spectroscopy study with evidence for graphite in olivine of ordinary chondrites. Meteorit. Planet. Sci. 53, 416-432. https://doi.org/10.1111/maps.13027

Kallemeyn, G.W., Rubin, A.E., Wasson, J.T., 1989. Compositional classification of chondrites: II. The iron-rich carbonaceous chondrites. Geochim. Cosmochim. Acta 53, 2747–2767.

Kerr, R.A., 2013. Meteorite mystery edges closer to an answer-or the end of a field. Science 341, 126-127.

Kuebler, K.E., Jolliff, B.L., Wang, A., Haskin, L.A., 2006. Extracting olivine (Fo–Fa) compositions from Raman spectral peak positions. Geochim. Cosmochim. Acta 70, 6201–6222. https://doi.org/10.1016/j.gca.2006.07.035

Lee, M.R., Bland, P.A., 2004. Mechanisms of weathering of meteorites recovered from hot and cold deserts and the formation of phyllosilicates. Geochim. Cosmochim. Acta 68, 893-916. https://doi.org/10.1016/S0016-7037(03)00486-1

Lewis, R.S., Tang, M., Wacker, J.F., Anders, E., Steel, E., 1987. Interstellar diamonds in meteorites. Nature 326, 160-162.

Lukačević, I., Gupta, S.K., Jha, P.K., Kirin. D., 2012. Lattice dynamics and Raman spectrum of rutile TiO_2: The role of soft phonon modes in pressure induced phase transition. Mater. Chem. Phys. 137, 282–289. https://doi.org/10.1016/J.MATCHEMPHYS.2012.09.022

Lv, T., Zhao, J., Chen, M., Shen, K., Zhang, D., Zhang, J. Zhang, G., Liu, Q., 2018. Boosted visible-light photodegradation of methylene blue by V and Co co-doped TiO_2. Materials 11, 1946. https://doi.org/10.3390/ma11101946

Ma, H.L., Yang, J.Y., Dai, Y., Zhang, Y.B., Lu, B., Ma, G.H., 2007. Raman study of phase transformation of TiO_2 rutile single crystal irradiated by infrared femtosecond laser. Appl. Surf. Sci. 253, 7497–7500. https://doi.org/10.1016/J.APSUSC.2007.03.047

Mahajan, R.R., 2017. Noble gases, nitrogen and cosmic ray exposure age of the Sulagiri Chondrite. Geosci. Front. 8, 205-210. http://dx.doi.org/10.1016/j.gsf.2015.12.010

570 Marshall, C.P., Edwards, H.G.M., Jehlicka, J., 2010. Understanding the application of Raman
571 spectroscopy to the detection of traces of life. Astrobiology 10, 229-243.
572 https://doi.org/10.1089/ast.2009.0344

573 Matson, D.W., Sharma, S.K., Philpotts, J.A., 1986. Raman spectra of some tectosilicates and
574 of glasses along the orthoclase-anorthite and nepheline-anorthite joins. Am. Mineral.
575 71, 694-704.

576 McSween, H.Y., 1999. Meteorites and Their Parent Planets, 2nd ed. Cambridge University
577 Press, London, 324pp.

578 Miyamoto, M., 1998. Micro-Raman spectroscopy of diamonds in the Canyon Diablo iron
579 meteorite: Implication for the shock origin. Antarct. Meteor. Res. 11, 171–177.

580 Mostefaoui, D., El Goresy, A., Hoppe, P., Gillet, P., Ott, U., 2002. Mode of occurrence, textural
581 settings and nitrogen isotopic compositions of in situ diamonds and other carbon
582 phases in the Bencubbin meteorite. Earth Planet. Sci. Lett. 204, 89–100.
583 https://doi.org/10.1016/S0012-821X(02)00964-0

584 Mouri, T., Enami, M., 2008. Raman spectroscopic study of olivine group minerals. J Mineral.
585 Petrol. Sci. 103, 100–104.

586 Ohsaka, T., Izumi, F., Fujiki, Y., 1978. Raman spectrum of anatase, TiO_2. J. Raman Spectrosc.
587 7, 321–324. https://doi.org/10.1002/jrs.1250070606

588 Ott,U., 1993. Interstellar grains in meteorites, Nature 364, 25-33.

589 Paliwal, B.S., Sisodia, M.S., Tripathi, R.P., 2002. Bhawad L(LL)6 chondrite: Petrography and
590 Mössbauer study. Curr. Sci. 83, 1071-1072.

591 Parker, J.C., Siegel, R.W., 1990. Calibration of the Raman spectrum to the oxygen
592 stoichiometry of nanophase TiO_2. Appl. Phys. Lett. 57, 943–945.
593 https://doi.org/10.1063/1.104274

594 Parthasarathy, G., Sharma, S.R., 2004. High-temperature electrical and thermal properties of
595 Burdett, Dalhart, Faucet, and Wellman ordinary chondrites. Curr. Sci. 86, 1366-1368.

596 Pittarello, L., Baert, K., Debaille, V., Claeys, P., 2015. Screening and classification of ordinary
597 chondrites by Raman spectroscopy. Meteorit. Planet. Sci. 50, 1718–1732.

598 https://doi.org/10.1111/maps.12506

599 Porto, S.P.S., Fleury, P.A., Damen, T.C., 1967. Raman spectra of TiO_2, MgF_2, ZnF_2, FeF_2, and
600 MnF_2. Phys. Rev. 154, 522–526. https://doi.org/10.1103/PhysRev. 154.522

601 Rubin A.E. 1992. A shock-metamorphic model for silicate darkening and compositionally
602 variable plagioclase in CK and ordinary chondrites. Geochim. Cosmochim. Acta 56,
603 1705–1714.

604 Rubin A.E. 1995. Petrologic evidence for collisional heating of chondritic asteroids. Icarus
605 113, 156–167.

606 Saikia, B.J., Parthasarathy, G., Sarmah, N.C., 2009a. Fourier transform infrared spectroscopic
607 characterization of Dergaon H5 chondrite: Evidence of aliphatic organic compound.
608 Nat. Sci. 7, 45-51.

609 Saikia, B.J., Parthasarathy, G., Sarmah, N.C., 2009b. Spectroscopic characterization of olivine
610 [$(Fe, Mg)_2 SiO_4$] in Mahadevpur H4/5 ordinary chondrite. J. Am. Sci. 5, 71–78.

611 Saikia, B.J., Parthasarathy, G., 2009c. Spectroscopic investigation of Mahadevpur H4/5
612 ordinary chondrite. Geochim. Cosmochim. Acta 73, 1144.

613 Saikia, B.J., Parthasarathy, G., Borah, R.R., 2017a. Nanodiamonds and silicate minerals in
614 ordinary chondrites as determined by micro-Raman spectroscopy. Meteorit. Planet.
615 Sci. 52, 1146–1154. https://doi.org/10.1111/maps.12850

616 Saikia, B.J., Parthasarathy, G., Borah, R.R., Satyanarayanan, M., Borthakur, R., Chetia, P.,
617 2017b. Spectroscopy and mineralogy of a fresh meteorite fall Kamargaon (L6)
618 chondrite. Proc. Indian National Sci. Acad. 83, 941-948.

619 https://doi.org/10.16943/ptinsa/2017/49124

620 Saikia, B.J., Parthasarathy, G., and Borah, R.R., 2017c. Mineralogy of meteorites from the
621 North-eastern India: A brief review. Geomaterials 7, 83–95.

622 https://doi.org/10.4236/gm.2017.73007

623 Saikia, B.J., Parthasarathy, G., Borah, R.R., Borthakur, R., Sarmah, A.J.D., 2017d. Meteorite
624 fall at Sadiya, India: A Raman spectroscopic classification. J. Astrophys. Aerosp.
625 Technol. 5, 1000149. https://doi.org/10.4172/2329-6542.1000149

626 Saikia, B.J., Parthasarathy, G., Borah, R.R., 2018a. Raman and Infrared spectroscopic tentative
627 identification of organic traces in Sadiya (LL5) ordinary chondrite. Ad. Ast. 3, 250-
628 256. https://dx.doi.org/10.22606/adap.2018.34004

629 Saikia, B.J., Parthasarathy, G., Borah, R.R., 2018b. Silicates in Kamargaon (L6) chondrite: A
630 Raman spectroscopic study. O. A. J. Math. Theor. Phys. 1, 225-230.

631 Saikia, B.J., 2020. Ordinary Chondrites from North-East India: A Raman and Infrared
632 Spectroscopic Approach, Cambridge Scholars Publishing, UK, 148pp.

633 Saikia, B.J., Parthasarathy, G., Borah, R.R., 2022a. High-pressure polymorphs of olivine and
634 silica in Kamargaon (L6) chondrite by laser micro-Raman and XRD studies. J. Earth
635 Syst. Sci. 131, 38. https://doi.org/10.1007/s12040-021-01803-y

636 Saikia, B.J., Parthasarathy, G., Chalapathi Rao, N.V., Borah, R.R., Kumar, D., 2022b. High
637 shock pressure metamorphism induced transformations of olivine and feldspar in
638 Natun Balijan L4 chondrite: Evidence from micro-raman, infrared spectroscopy, x-
639 ray diffraction and electron microprobe analysis. Jour. Geol. Soc. India 98, 731-739.
640 https://doi.org/10.1007/s12594-022-2061-7

641 Saikia, B.J., Basak, S., Borah, R.R., Parthasarathy, G., 2022c. Spectroscopic investigations and
642 mineral chemistry of dunite from the sargur supracrustals (3 Ga) greenstone belt:

643 Implications to terrestrial analogues for lunar and martian dunite. Jour. Geol. Soc.
644 India 98, 1505-1512. https://doi.org/10.1007/s12594-022-2205-9

645 Saikia, B.J., Parthasarathy, G., Chalapathi Rao, N.V., Seth, V., Borah, R.R., 2024. Mineral
646 chemistry of Mahadevpur H4/5 chondrite: characterization of nanodiamonds through
647 micro-Raman spectroscopic studies. Curr. Sci. 126, 574-582.

648 https://doi.org/10.18520/cs/v126/i5/574-582

649 Sekiya, T., Ohta, S., Kamei, S., Hanakawa, M., Kurita, S., 2001. Raman spectroscopy and
650 phase transition of anatase TiO_2 under high pressure. J. Phys. Chem. Solids 62,717–
651 721. https://doi.org/10.1016/S0022-3697(00)00229-8

652 Smith, F.C., Glass, B.P., Simonson, B.M., Booksh, K.S., 2016. Shock-metamorphosed rutile
653 grains containing the high-pressure polymorph TiO_2-II in four Neoarchean spherule
654 layers. Geology 44, 775–778.

655 Stöffler, D., Keil, K., Scott, E.R.D., 1991. Shock metamorphism of ordinary chondrites.
656 Geochim. Cosmochim. Acta 55, 3845–3867.

657 Swamy, V., Muddle, B.C., Dai, Q., 2006. Size-dependent modifications of the Raman spectrum
658 of rutile TiO_2. Appl. Phys. Lett. 89, 163118 https://doi.org/10.1063/1.2364123

659 Tompsett, G.A., Bowmaker, G.A., Cooney, R.P., Metson, J.B., Rodgers, K.A., Seakins, J.M.,
660 1995. The Raman spectrum of brookite, TiO_2 (Pbca, Z = 8). J. Raman Spectrosc. 26,
661 57–62. https://doi.org/10.1002/jrs.1250260110

662 Wang, A., Kuebler, K.E., Jolliff, B.L., Haskin, L.A., 2004. Raman spectroscopy of Fe–Ti–Cr-
663 oxides, case study: Martian meteorite EETA79001. Am. Mineral. 89, 665–680.
664 https://doi.org/10.2138/am-2004-5-601

665 Wasson, J.T., Kallemeyn, G.W., 1988. Composition of chondrites. Philos. Trans. R. Soc.
666 London A 325, 535–544.

667 Wasson, T., 1974. Meteorites, Classification and Properties. Springer Verlag, New York ,
668 185pp.

669 Wopenka, B., Xu, Y. C., Zinner, E., Amari, S., 2013. Murchison presolar carbon grains of
670 different density fractions: A raman spectroscopic perspective. Geochim.
671 Cosmochim. Acta 106, 463–489.

672 Yan, J., Wu, G., Guan, N., Li, L., Li, Z., Cao, X., 2013. Understanding the effect of surface/bulk
673 defects on the photocatalytic activity of TiO_2: anatase versus rutile. Phys. Chem.
674 Chem. Phys. 15, 10978. https://doi.org/10.1039/c3cp50927c

675 Yu,Y.G., Wentzcovitch, R.M., 2006. Density functional study of vibrational and
676 thermodynamic properties of ringwoodite. J. Geophys. Res. 111, B12202.
677 https://doi.org/10.1029/2006JB004282

678 Zhang, J., Li, M., Feng, Z., Chen, J., Li, C., 2006. UV Raman spectroscopic study on TiO_2. I.
679 Phase Transformation at the Surface and in the Bulk. J. Phys. Chem. 110, 927-935.
680 https://doi.org/10.1021/JP0552473

Zhang, Y., Harris, C.X., Wallenmeyer, P., Murowchick, J., Chen, X., 2013. Asymmetric lattice vibrational characteristics of rutile TiO_2 as revealed by laser power dependent Raman spectroscopy. J. Phys. Chem. C. 117, 24015–24022. https://doi.org/10.1021/jp406948e

Figure Captions

Fig. 1. FF HRTEM images of Bhawad meteorite (a) 200 nm, (b) 100 nm, (c) 50 nm, (d) 20 nm, (e) 10 nm, (f) 5 nm.

Fig. 2 (a) HRTEM image showing d-space at different lattice fringes within 5 nm, (b) distance between a number of crystal fringes through inverse FFT for evaluation of d-space, (c) gray value intensity profile indicating the number and positions of fringes based on peak counts.

Fig. 3. (a) d-spacing values calculated from the selected area electron diffraction (SAED) pattern obtained through HRTEM analysis; (b) corresponding gray value intensity profile derived from the SAED pattern.

Fig. 4. Raman spectrum of the Bhawad chondrite showing the characteristic olivine doublet at 819 and 851 cm^{-1}.

Fig. 5. Raman spectrum of the Bhawad chondrite exhibiting characteristic pyroxene peaks.

Fig.6. Raman spectrum of the Bhawad chondrite showing characteristic features of plagioclase.

Fig.7. Raman spectrum of the chromite phase in the Bhawad chondrite.

Fig.8. Raman spectra of carbonaceous material associated with accessory phases in the Bhawad chondrite.

713

714 **Fig.9.** Raman spectrum revealing high-pressure titanium dioxide (TiO_2) polymorphs coexisting
715 with carbonaceous material and accessory phases in the Bhawad chondrite.

716

717 **Fig.10.** Raman spectrum depicts characteristic of chemically heterogeneous glass in the
718 Bhawad chondrite.

719